Multirow Adjoint-Based Optimization of NICFD Turbomachinery Using a Computer-Aided Design-Based Parametrization

Agromayor, Roberto; Anand, N.; Pini, M.; O. Nord, Lars

DOI
10.1115/1.4052881

Publication date
2022

Document Version
Final published version

Published in
Journal of Engineering for Gas Turbines and Power

Citation (APA)
Agromayor, R., Anand, N., Pini, M., & O. Nord, L. (2022). Multirow Adjoint-Based Optimization of NICFD Turbomachinery Using a Computer-Aided Design-Based Parametrization. *Journal of Engineering for Gas Turbines and Power*, *144*(4), 1-15. Article 041008. https://doi.org/10.1115/1.4052881

Roberto Agromayor[1]
Department of Energy and Process Engineering,
NTNU—The Norwegian University of Science
and Technology,
Kolbj. Hejes v. 1B,
Trondheim NO-7491, Norway
e-mail: roberto.agromayor@ntnu.no

Nitish Anand
Propulsion & Power,
Aerospace Engineering Faculty,
Delft University of Technology,
Kluyverweg 1,
Delft 2629 HS, The Netherlands
e-mail: n.anand@tudelft.nl

Matteo Pini
Propulsion & Power,
Aerospace Engineering Faculty,
Delft University of Technology,
Kluyverweg 1,
Delft 2629 HS, The Netherlands
e-mail: m.pini@tudelft.nl

Lars O. Nord
Department of Energy and Process Engineering,
NTNU—The Norwegian University of Science
and Technology,
Kolbj. Hejes v. 1B,
Trondheim NO-7491, Norway
e-mail: lars.nord@ntnu.no

Multirow Adjoint-Based Optimization of NICFD Turbomachinery Using a Computer-Aided Design-Based Parametrization

Currently, most of the adjoint-based design systems documented in the open literature assume that the fluid behaves as an ideal gas, are restricted to the optimization of a single row of blades, or are not suited to impose geometric constraints. In response to these limitations, this paper presents a gradient-based shape optimization framework for the aerodynamic design of turbomachinery blades operating under nonideal thermodynamic conditions. The proposed design system supports the optimization of multiple blade rows, and it integrates a computer-aided design (CAD)-based parametrization with a Reynolds-averaged Navier–Stokes (RANS) flow solver and its discrete adjoint counterpart. The capabilities of the method were demonstrated by performing the design optimization of a single-stage axial turbine that employs isobutane (R600a) as working fluid. Notably, the aerodynamic optimization respected the minimum thickness constraint at the trailing edge of the stator and rotor blades and reduced the entropy generation within the turbine by 36%, relative to the baseline, which corresponds to a total-to-total isentropic efficiency increase of about 4 percentage points. The analysis of the flow field revealed that the performance improvement was achieved due to the reduction of the wake intensity downstream of the blades and the elimination of a shock-induced separation bubble at the suction side of the stator cascade. [DOI: 10.1115/1.4052881]

1 Introduction

Automated design workflows are emerging as a powerful tool for the aerodynamic design of turbomachinery components [1]. These workflows integrate geometry parametrization tools, high-fidelity physical models, and numerical optimization techniques, and they enable the exploration of large design spaces in a systematic way [1]. This, in turn, allows the designer to obtain higher performance gains and shorten the development time with respect to traditional design workflows based on trial-and-error [2]. Moreover, automated design workflows offer a great potential for unconventional turbomachinery applications, for which a large body of previous design experience does not yet exist. Examples of these applications include turbomachines operating in the nonideal compressible fluid dynamics (NICFD) regime [3], such as organic Rankine cycle turbines [4–6], supercritical carbon dioxide turbines and compressors [7,8], or refrigeration and heat pump turbocompressors [9,10].

The optimization methods used within automated workflows can be classified according to the use of derivative information as gradient-free or gradient-based. Gradient-free methods only require the evaluation of the cost function values, and they are widely used due to their robustness, simple integration with black-box models, and ability to handle nonsmooth or even discontinuous optimization problems [11]. Over the years, gradient-free methods have been successfully applied for the aerodynamic design of turbines [6,12,13] and compressors [14,15]. However, these methods require a large number of function evaluations to converge to the optimum solution, especially when the number of design variables is large. This, in turn, results in high computational cost, which hampers the widespread application of gradient-free methods to complex industrial design problems [16]. Gradient-based methods, on the other hand, are particularly suited to solve differentiable problems involving a large number of design variables [17]. These methods require not only the values but also the gradients of the cost functions, and they usually converge to the optimum solution in a comparatively low number of iterations. Consequently, the aerodynamic design of turbomachinery, which usually involves a large number of design variables, may benefit significantly from the development of efficient gradient-based optimization methods [16].

In the context of fluid-dynamic shape optimization, the adjoint method has emerged as a very efficient way to evaluate the gradient of a cost function with respect to an arbitrary number of design variables [18,19]. The application of this method to external aerodynamics was pioneered by Pironneau [20] and later revisited and extended by Jameson and co-workers, who used it to optimize airfoils, wings, and complete aircraft configurations [21–23]. By contrast, the application of the adjoint method to turbomachinery design has lagged behind, arguably, due to the additional complexity involved in the derivation of the adjoint equations and boundary conditions for internal flow problems. As reported in Table 1, most of the applications of the adjoint method were limited to the optimization of a single row of blades and used the assumption of constant eddy viscosity (CEV) to avoid the challenges associated with the differentiation of mixing-plane boundary conditions and turbulence models [55]. In addition, with the exception of few recent and notable works [38,47,54,55], all flow and adjoint solvers assume that the fluid obeys the perfect gas law, preventing their application to NICFD problems where the thermophysical properties of the fluid are calculated with complex equations of state.

Alongside with the choice of optimization method, the performance achieved during the aerodynamic design is largely dependent

---

[1] Corresponding author.

Manuscript received June 27, 2021; final manuscript received October 12, 2021; published online January 21, 2022. Assoc. Editor: Ernesto Benini.

Table 1 Survey of publications using the adjoint method for thermal turbomachinery design optimization

Reference		Dimensions[a]	Flow	Adjoint[b]	CEV	Flow state	Blade rows	Parametrization[c]
Yang et al. (2003)	[24]	2D	Euler	Continuous	—	Ideal	Single	Mesh
Wu et al. (2003)	[25]	2D	Euler	Continuous	—	Ideal	Single	Mesh
Wu et al. (2005)	[26]	3D	RANS	Continuous	Yes	Ideal	Single	Mesh
Arens et al. (2005)	[27]	2D	Euler	Continuous	—	Ideal	Single	CAD[d]
Li et al. (2006)	[28]	2D	Euler	Continuous	—	Ideal	Single	CAD[d]
Papadimitriou and Giannakoglou (2006)	[29]	3D	RANS	Continuous	Yes	Ideal	Single	CAD[d]
Papadimitriou and Giannakoglou (2006)	[29]	3D	RANS	Continuous	Yes	Ideal	Single	CAD[d]
Duta et al. (2007)	[30]	3D	RANS	Discrete	No	Ideal	Single	CAD
Corral and Gisbert (2008)	[31]	3D	RANS	Discrete	Yes	Ideal	Single	Mesh
Wang and He (2010)	[32]	3D	RANS	Continuous	Yes	Ideal	Multi	Mesh
Wang et al. (2010)	[33]	3D	RANS	Continuous	Yes	Ideal	Multi	Mesh
Luo et al. (2011)	[34]	3D	Euler	Continuous	—	Ideal	Single	Mesh
Walther and Nadarajah (2013)	[35]	2D	RANS	Discrete	Yes	Ideal	Multi	Mesh
Luo et al. (2014)	[36]	3D	RANS	Continuous	Yes	Ideal	Single	Mesh
Walther and Nadarajah (2014)	[37]	3D	RANS	Discrete	Yes	Ideal	Multi	Mesh
Pini et al. (2015)	[38]	2D	Euler	Discrete	—	Nonideal	Single	CAD[d]
Xu et al. (2015)	[39]	3D	RANS	Discrete	No	Ideal	Multi	CAD[d]
Montanelli et al. (2015)	[40]	2D	RANS	Discrete	Yes	Ideal	Single	CAD
Luo et al. (2015)	[41]	3D	RANS	Continuous	Yes	Ideal	Single	Mesh
Walther and Nadarajah (2015)	[42]	2D	RANS	Discrete	Yes	Ideal	Multi	Mesh
Walther and Nadarajah (2015)	[43]	3D	RANS	Discrete	Yes	Ideal	Multi	Mesh
Walther and Nadarajah (2015)	[44]	3D	RANS	Discrete	Yes	Ideal	Multi	Mesh
Tang et al. (2018)	[45]	3D	RANS	Discrete	Yes	Ideal	Single	Mesh
Müller and Verstraete (2017)	[46]	3D	RANS	Discrete	Yes	Ideal	Single	CAD
Vitale et al. (2017)	[47]	2D	RANS	Discrete	No	Nonideal	Single	Mesh
Luers et al. (2018)	[48]	3D	RANS	Discrete	No	Ideal	Single	CAD[d]
Anand et al. (2018)	[49]	2D	RANS	Discrete	No	Ideal	Single	Both
Mykhaskiv et al. (2018)	[50]	3D	RANS	Discrete	No	Ideal	Single	CAD
Sanchez Torreguitart et al. (2018)	[51]	2D	RANS	Discrete	Yes	Ideal	Single	CAD
Sanchez Torreguitart et al. (2019)	[52]	2D	RANS	Discrete	Yes	Ideal	Single	CAD
Russo et al. (2019)	[53]	2D	RANS	Discrete	Yes	Ideal	Single	CAD
Rubino et al. (2020)	[54]	2D	RANS	Discrete	No	Nonideal	Multi	Mesh
Vitale et al. (2020)	[55]	3D	RANS	Discrete	No	Nonideal	Multi	Mesh
Present work		2D	RANS	Discrete	No	Nonideal	Multi	CAD

[a] Number of dimensions of the problem, two-dimensional (2D) or three-dimensional (3D).
[b] Type of adjoint formulation, continuous or discrete.
[c] Type of geometry parametrization, mesh-based or CAD-based.
[d] This work uses the control points of the NURBS curves or surfaces that define the geometry as design variables. For this special case, the derivatives of the surface displacements can be computed analytically in a simple way.

on the geometry parametrization that defines the design space containing the optimal solution [56]. In many cases, see Table 1, the geometry of the blades is updated at the level of the computational grid using mesh-based parametrization methods such as grid-point displacement [35,42], superposition of Hicks–Henne bumps [32,33], superposition of harmonic functions [31,41], free-form deformation morphing [47,55], or radial basis function interpolation morphing [45]. Although these methods offer a lot of flexibility in terms of degrees-of-freedom of the blade shape, they are not well-suited for optimization problems involving geometric constraints (e.g., minimum trailing edge thickness) [47,55]. In addition, the optimized shape only exists as a surface mesh that needs to be transferred back to a computer-aided design (CAD) format for further analysis or manufacturing. The reconstruction of the CAD-model from the surface mesh, albeit possible, is not a straightforward process, and it may introduce fitting errors that can have a detrimental impact on the fluid-dynamic performance of the resulting geometry [57,58]. As an alternative, CAD-based parametrization methods maintain a consistent CAD representation of the geometry at every design iteration and, as a result, the optimal shape is directly available in a format compatible with CAD tools [39,50]. Moreover, these methods allow the designer to impose geometric constraints in a natural and nonintrusive way, giving more control over the shape to be optimized [46,50]. Despite their advantages, CAD-based parametrizations are not widely applied in combination with gradient-based optimization methods. This is possibly due to the challenges associated with the calculation of the shape sensitivities with respect to the design variables controlling the CAD model [58,59].

As summarized in Table 1, the majority of automated design systems relying on the adjoint method assume that the fluid behaves as an ideal gas, are restricted to the optimization of a single row of blades, or use mesh-based parametrizations that are not suited to impose geometric constraints. Recently, Vitale et al. [47] developed a discrete adjoint solver for NICFD applications, which was subsequently extended to multistage turbomachinery configurations and integrated into the SU2 shape optimization framework [55]. Despite the merits of the method, the geometry of the blades

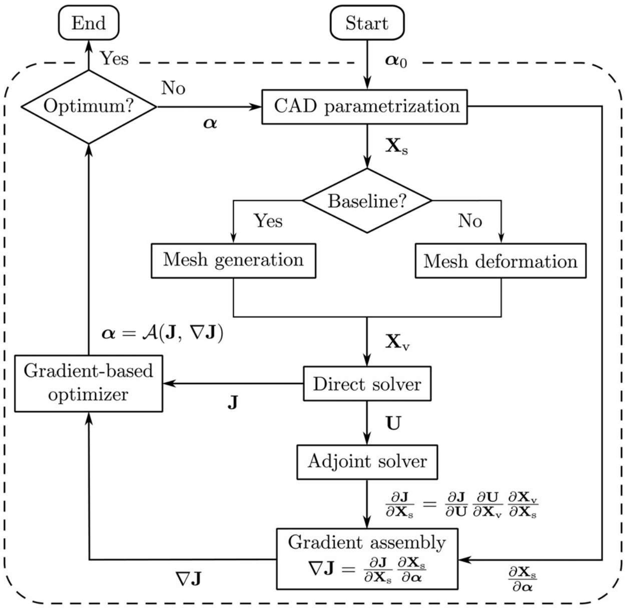

Fig. 1 Outline of the optimization framework used to carry out the aerodynamic design

Table 2 Design variables of the parametric CAD model

Variable name	Symbol
Spacing	s
Axial chord	c_{ax}
Stagger angle	ξ
Inlet and exit metal angles	θ_{in}, θ_{out}
Inlet and exit tangent proportions	d_{in}, d_{out}
Inlet and exit radii of curvature	r_{in}, r_{out}
Upper and lower thickness distributions[a]	t^{u}, t^{l}

[a]Each thickness distribution is a cubic B-spline polynomial defined by six control points.

is parametrized by means of free-form deformation boxes. Consequently, it is challenging to impose geometric constraints and obtain manufacturable blade shapes out of the optimization process [55].

In response to this limitation, this paper documents the development of an improved gradient-based shape optimization framework for the aerodynamic design of turbomachinery blades operating with nonideal flows, i.e., in the NICFD regime. The proposed design system integrates a recently developed CAD-based parametrization method [58] with the discrete adjoint solver documented in Ref. [55]. By virtue of the CAD-based parametrization, the proposed framework is suited for an effective handling of geometric constraints such as minimum trailing edge thickness or constant axial chord. The capabilities of the method were demonstrated by performing the design optimization of a single-stage axial turbine operating with isobutane (R600a) as working fluid. This turbine is going to be manufactured and tested in the EXPAND facility [60] at the Norwegian University of Science and Technology with the aim to provide experimental datasets that contribute toward the validation and refinement of the models currently in use for the design and analysis of organic Rankine cycle turbines.

2 Methodology

The proposed aerodynamic design method is based on the shape optimization framework illustrated in Fig. 1. The design system enables the solution of constrained and unconstrained turbomachinery design problems involving one or multiple blade rows, and it integrates a CAD-based parametrization tool, mesh generation and deformation routines, a NICFD turbomachinery flow solver and its discrete adjoint counterpart, and a gradient-based optimization algorithm that drives the design process. In what follows, the components of the optimization framework are described in detail.

2.1 Computer-Aided Design-Based Blade Shape Parametrization. The geometry of the blades is described using the CAD-based parametrization method documented in Refs. [58] and [61]. This method uses engineering design variables (leading/trailing edge radius, metal angles, blade thickness, etc.) and nonuniform rational basis spline (NURBS) curves [62] to represent the geometry of the blades. The design variables used to define one row of blades in two dimensions are listed in Table 2. In contrast with most of the two-dimensional (2D) methods available in the open literature [58], this parametrization produces blade profiles that have continuous curvature and rate of change of curvature by construction. This feature is important to avoid discontinuities in the surface pressure distribution that may lead to flow separation [63].

The construction of one blade profile and flow domain is illustrated in Fig. 2. First, the camber-line is determined given the axial chord $c_{\mathrm{ax}} = c \cos \xi$, stagger angle ξ, metal angles θ_{in} and θ_{out}, and tangent proportions d_{in} and d_{out}. After that, two independent thickness distributions t^{u} and t^{l} are imposed normal to the camber-line to define the upper and lower sides of the blade. The normal distance for the first and last control points is computed using the end-point curvature equations for NURBS curves [58] to prescribe the radius of curvature at the leading and trailing edges r_{in} and r_{out}. Finally, the flow domain is defined by the inflow and outflow boundaries as well as the two periodic boundaries located an offset distance of half of the blade spacing s with respect to the blade camber-line.

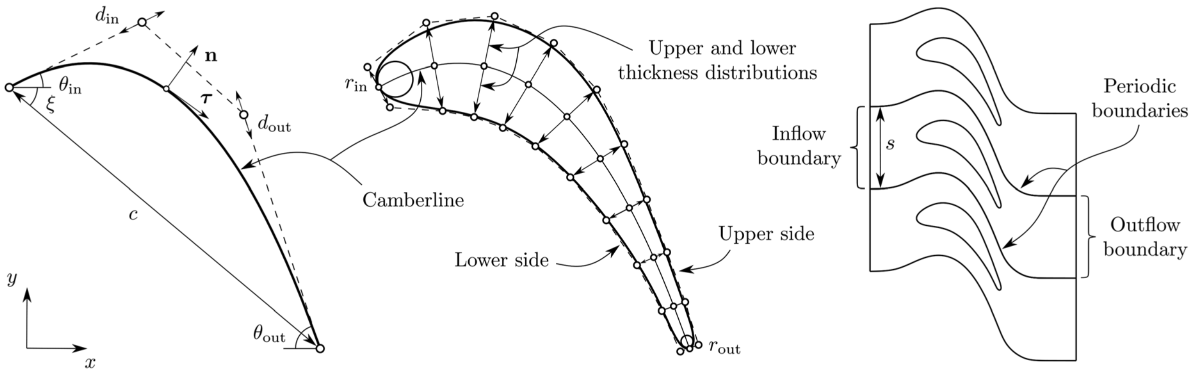

Fig. 2 Outline of the CAD-based parametrization method used to generate the geometry of a blade cascade

2.2 Mesh Generation and Deformation. The flow domain corresponding to the baseline CAD model is discretized using unstructured grids by means of the GMSH meshing tool [64,65]. The mesh is only generated once for the baseline geometry and then deformed each time that the design variables from the CAD parametrization are updated at each optimization step. To this aim, the baseline blade coordinates are mapped into the CAD model using the point projection method described in Ref. [58]. Then, at each optimization step, the deformation of the blade boundary (i.e., the difference between the updated and initial blade coordinates) is propagated into the flow domain using a linear-elasticity mesh deformation method [66]. This approach was adopted instead of recreating the mesh at each design step because the latter would change the topology of the unstructured mesh, affect the discretization error of the flow solution, and deteriorate the convergence rate of the optimization algorithm [66].

2.3 Flow Solver. The flow is described by the compressible Reynolds-averaged Navier–Stokes (RANS) equations [67]. Following the absolute velocity formulation, the RANS equations for a rotating frame of reference with constant angular velocity $\mathbf{\Omega}$ can be expressed in differential and conservative form as

$$\frac{\partial \mathbf{U}}{\partial t} + \nabla \cdot (\mathbf{F}^{\mathrm{c}} - \mathbf{F}^{\mathrm{v}}) - \mathbf{S} = 0 \tag{1}$$

where the vector of conservative variables $\mathbf{U}$, vector of convective fluxes $\mathbf{F}^{\mathrm{c}}$, vector of viscous fluxes $\mathbf{F}^{\mathrm{v}}$, and source term $\mathbf{S}$ arising due to Coriolis acceleration are given by

$$\begin{aligned} \mathbf{U} &= \begin{bmatrix} \rho \\ \rho\,\mathbf{v} \\ \rho E \end{bmatrix}, \quad \mathbf{F}^{\mathrm{c}} = \begin{bmatrix} \rho\,\mathbf{w} \\ \rho\,\mathbf{v} \otimes \mathbf{w} + p\,\mathbf{I} \\ \rho E\,\mathbf{w} + p\,\mathbf{v} \end{bmatrix}, \\ \mathbf{F}^{\mathrm{v}} &= \begin{bmatrix} 0 \\ \boldsymbol{\tau} \\ \boldsymbol{\tau} \cdot \mathbf{v} - \dot{\mathbf{q}} \end{bmatrix}, \quad \text{and} \quad \mathbf{S} = \begin{bmatrix} 0 \\ -\rho\,\mathbf{\Omega} \times \mathbf{v} \\ 0 \end{bmatrix} \end{aligned} \tag{2}$$

In these equations, ρ is the fluid density, p is the static pressure, T is the static temperature, $E = e + (\mathbf{v} \cdot \mathbf{v})/2$ is the total energy, and e is the specific internal energy. The density and specific internal energy are utilized as the independent thermodynamic variables, while the rest of the fluid properties are computed using the Peng–Robinson equation of state [68,69]. Moreover, the absolute velocity vector $\mathbf{v}$ is defined as the sum of the relative velocity $\mathbf{w}$ and the velocity of the rotating frame of reference $\mathbf{\Omega} \times \mathbf{X}$. Assuming that the fluid is Newtonian and that the Stokes' hypothesis holds [70, pp. 62–67], the viscous stress tensor is given by

$$\boldsymbol{\tau} = (\mu + \mu_{\mathrm{t}}) \left[\nabla \mathbf{v} + \nabla \mathbf{v}^{\mathrm{T}} - \frac{2}{3} (\nabla \cdot \mathbf{v})\, \mathbf{I} \right] \tag{3}$$

where μ is the molecular viscosity and μ_{t} is the turbulence viscosity, which is computed utilizing the two-equation shear stress transport turbulence model proposed by Menter [71]. Similarly, the heat flux is given by $\dot{\mathbf{q}} = -(k + k_{\mathrm{t}})\, \nabla T$, where k is the molecular thermal conductivity and k_{t} is the turbulence thermal conductivity.

The continuous partial differential equations governing the flow are discretized in space using an unstructured, vertex-based finite volume method [72] within the SU2 multiphysics software tool [73,74]. The semidiscretized integral form of the RANS equations is expressed as

$$\Delta V_i \frac{\mathrm{d}\mathbf{U}_i}{\mathrm{d}t} + \sum_j (\mathbf{F}^{\mathrm{c}}_{ij} - \mathbf{F}^{\mathrm{v}}_{ij}) \Delta S_{ij} - \Delta V_i\, \mathbf{S}_i = 0 \tag{4}$$

$$\Delta V_i \frac{\mathrm{d}\mathbf{U}_i}{\mathrm{d}t} + \mathbf{R}_i(\mathbf{U}) = 0 \tag{5}$$

where $\mathbf{U}_i$ is the flow solution at node i, $\mathbf{R}_i$ is the numerical residual, $\mathbf{F}^{\mathrm{c}}_{ij,}$ and $\mathbf{F}^{\mathrm{v}}_{ij}$ are the numerical convective and viscous fluxes, respectively, $\mathbf{S}_i$ is a uniform reconstruction of the source term, ΔV_i is the volume of the dual control volume, and ΔS_{ij} is the area of the face associated with the edge ij. The convective fluxes for nonideal compressible flows are computed using a generalized version of Roe's approximate Riemann solver [75,76], and the numerical dissipation is controlled with the entropy fix proposed by Harten and Hyman [77]. A monotonic upstream-centered scheme for conservation laws linear reconstruction [78] is used to achieve second-order accuracy in space, and the van Albada slope limiter [79,80] is adopted to suppress oscillations near discontinuities such as shock waves. In addition, the convective fluxes of the turbulence model are computed using a first-order scalar upwind scheme, and all viscous fluxes are evaluated using a corrected average-gradient method [81]. The gradients of the flow variables needed to evaluate the convective and viscous fluxes are calculated using the weighted least-squares method [82].

The steady-state solution of the RANS equations is computed with an implicit Euler pseudotime integration accelerated by local time-stepping [73]. The change of the conservative variables at each time-step is thus given by

$$\left(\frac{\Delta V_i}{\Delta t_i^n}\, \delta_{ij} + \frac{\partial \mathbf{R}_i(\mathbf{U}^n)}{\partial \mathbf{U}_j} \right) \Delta \mathbf{U}^n = \mathbf{P}\, \Delta \mathbf{U}^n = -\mathbf{R}(\mathbf{U}^n) \tag{6}$$

where $\Delta \mathbf{U}^n = \mathbf{U}^{n+1} - \mathbf{U}^n$, and δ_{ij} is the Kronecker delta function. This linear system can be written as a fixed-point equation, yielding

$$\mathbf{U}^{n+1} = \mathbf{U}^n - \mathbf{P}^{-1}\, \mathbf{R}(\mathbf{U}^n) = \mathbf{G}(\mathbf{U}^n) \tag{7}$$

where $\mathbf{G}$ is the fixed-point operator. The product $\mathbf{P}^{-1}\, \mathbf{R}$ is computed by solving the sparse linear system given by Eq. (6) using a flexible generalized minimal residual method [83, pp. 171–193] preconditioned by an incomplete lower-upper factorization with no filling [83, pp. 301–319].

An adiabatic, nonslip wall boundary condition is used at the surface of the blades. In addition, the inflow and outflow boundaries use an extension of the characteristic-based, nonreflecting boundary conditions proposed by Giles [84,85] generalized to fluids described by arbitrary equations of state [47]. The total pressure, total temperature, flow direction, turbulence intensity, and viscosity ratio are specified at the inlet of the first blade row, whereas the static pressure was prescribed at the exit of the last blade row. The stator and rotor flow domains are coupled using the conservative, nonreflecting mixing-plane interface proposed by Saxer and Giles [86,87] with the modifications suggested by Vitale et al. [55]. Finally, periodic boundary conditions are used to reduce the computational domain to a single blade per row.

2.4 Adjoint Solver and Gradient Evaluation. Once that the flow equations are solved, the objective function and constraints of the optimization problem (simply termed cost functions $\mathbf{J}$) are computed. In addition to their value, the gradient-based optimizer also requires their derivatives with respect to the design variables $\nabla \mathbf{J}$. The dependence of a scalar cost function J with respect to the design variables can be conceptually expressed as

$$\boldsymbol{\alpha} \rightarrow \mathbf{X}_{\mathrm{s}} \rightarrow \mathbf{X}_{\mathrm{v}} \rightarrow \mathbf{U} \rightarrow J$$

where $\boldsymbol{\alpha}$ is the set of design variables, $\mathbf{X}_{\mathrm{s}}$ are the blade surface mesh coordinates, $\mathbf{X}_{\mathrm{v}}$ are the volume mesh coordinates, and $\mathbf{U}$ is the flow solution vector.

The derivatives of the cost function with respect to the surface coordinates $\partial J / \partial \mathbf{X}_{\mathrm{s}}$, also called computational fluid dynamics (CFD) sensitivities, are computed using the discrete adjoint solver documented in Ref. [88]. The adjoint equations associated with the cost function J can be derived from the following optimization problem:

$$\text{minimize} \quad J(\mathbf{U}(\mathbf{X}_\mathrm{s}),\, \mathbf{X}_\mathrm{v}(\mathbf{X}_\mathrm{s})) \tag{8}$$

$$\text{subject to} \quad \mathbf{U}(\mathbf{X}_\mathrm{s}) = \mathbf{G}(\mathbf{U}(\mathbf{X}_\mathrm{s}),\, \mathbf{X}_\mathrm{v}(\mathbf{X}_\mathrm{s})) \tag{9}$$

$$\mathbf{X}_\mathrm{v}(\mathbf{X}_\mathrm{s}) = \mathbf{M}(\mathbf{X}_\mathrm{s}) \tag{10}$$

where Eqs. (9) and (10) are the constraints imposed by the discretized RANS equations and the mesh deformation equations, respectively. The Lagrangian function associated with this problem is given as

$$\begin{aligned} L = {} & J(\mathbf{U}(\mathbf{X}_\mathrm{s}),\, \mathbf{X}_\mathrm{v}(\mathbf{X}_\mathrm{s})) \\ & + (\mathbf{G}(\mathbf{U}(\mathbf{X}_\mathrm{s}),\, \mathbf{X}_\mathrm{v}(\mathbf{X}_\mathrm{s})) - \mathbf{U}(\mathbf{X}_\mathrm{s}))^\mathrm{T} \boldsymbol{\lambda} \\ & + (\mathbf{M}(\mathbf{X}_\mathrm{s}) - \mathbf{X}_\mathrm{v}(\mathbf{X}_\mathrm{s}))^\mathrm{T} \boldsymbol{\mu} \end{aligned} \tag{11}$$

where $\boldsymbol{\lambda}$ and $\boldsymbol{\mu}$ are the Lagrangian multipliers or adjoint variables of the problem. Using the chain rule of differentiation, the derivatives of the Lagrangian function with respect to the mesh surface coordinates are given by

$$\begin{aligned} \frac{\partial L}{\partial \mathbf{X}_\mathrm{s}} = {} & \left(\frac{\partial \mathbf{M}}{\partial \mathbf{X}_\mathrm{s}}\right)^\mathrm{T} \boldsymbol{\mu} \\ & + \left(\frac{\partial J}{\partial \mathbf{U}} + \left(\frac{\partial \mathbf{G}}{\partial \mathbf{U}}\right)^\mathrm{T} \boldsymbol{\lambda} - \boldsymbol{\lambda}\right) \frac{\partial \mathbf{U}}{\partial \mathbf{X}_\mathrm{s}} \\ & + \left(\frac{\partial J}{\partial \mathbf{X}_\mathrm{v}} + \left(\frac{\partial \mathbf{G}}{\partial \mathbf{X}_\mathrm{v}}\right)^\mathrm{T} \boldsymbol{\lambda} - \boldsymbol{\mu}\right) \frac{\partial \mathbf{X}_\mathrm{v}}{\partial \mathbf{X}_\mathrm{s}} \end{aligned} \tag{12}$$

from which the adjoint equations are derived as

$$\boldsymbol{\lambda} = \frac{\partial J}{\partial \mathbf{U}} + \left(\frac{\partial \mathbf{G}}{\partial \mathbf{U}}\right)^\mathrm{T} \boldsymbol{\lambda} \tag{13}$$

$$\boldsymbol{\mu} = \frac{\partial J}{\partial \mathbf{X}_\mathrm{v}} + \left(\frac{\partial \mathbf{G}}{\partial \mathbf{X}_\mathrm{v}}\right)^\mathrm{T} \boldsymbol{\lambda} \tag{14}$$

If the adjoint variables $\boldsymbol{\lambda}$ and $\boldsymbol{\mu}$ satisfy Eqs. (13) and (14), then the derivative of the Lagrangian function (and the cost function) with respect to the mesh surface coordinates is simply given by

$$\frac{\partial L}{\partial \mathbf{X}_\mathrm{s}} = \frac{\partial J}{\partial \mathbf{X}_\mathrm{s}} = \left(\frac{\partial \mathbf{M}}{\partial \mathbf{X}_\mathrm{s}}\right)^\mathrm{T} \boldsymbol{\mu} \tag{15}$$

In order to solve the adjoint equations, $\boldsymbol{\lambda}$ is computed from Eq. (13) using the fixed-point iteration

$$\boldsymbol{\lambda}^{n+1} = \frac{\partial J}{\partial \mathbf{U}} + \left(\frac{\partial \mathbf{G}}{\partial \mathbf{U}}\right)^\mathrm{T} \boldsymbol{\lambda}^n = \mathbf{N}(\boldsymbol{\lambda}^n) \tag{16}$$

and, after that, $\boldsymbol{\lambda}$ is used in Eq. (14) to obtain $\boldsymbol{\mu}$. One important feature of the discrete adjoint formulation is that the primal (flow) and dual (adjoint) fixed-point iterations satisfy

$$\left\| \frac{\partial \mathbf{N}}{\partial \boldsymbol{\lambda}} \right\| = \left\| \frac{\partial \mathbf{G}}{\partial U} \right\| \tag{17}$$

and, as a result, the convergence properties of the RANS solver are inherited by the adjoint solver [88].

All the partial derivatives of the adjoint system, Eqs. (13) and (14), are obtained by applying the CODIPACK algorithmic differentiation library [89,90] to the top-level routine of the RANS solver. In this way, all the features of the flow solver such as turbulence models, equations of state, and boundary conditions, including the mixing-plane interface, are automatically differentiated and made available in the adjoint solver. This differs with respect to the majority of adjoint solvers described in the open literature, which are derived by manual differentiation or by selective application of automatic differentiation and often rely on simplifying assumptions such as the CEV approximation to ease their development and implementation, see Table 1.

The last step of the differentiation chain is the computation of the derivatives of the mesh surface coordinates with respect to the design variables $\partial \mathbf{X}_\mathrm{s}/\partial \boldsymbol{\alpha}$. These derivatives, also called CAD sensitivities, are computed by applying the complex-step method [91–93] to the parametric CAD model

$$\frac{\partial \mathbf{X}_\mathrm{s}}{\partial \boldsymbol{\alpha}} = \frac{\mathrm{Im}\big(\mathbf{X}_\mathrm{s}(\boldsymbol{\alpha} + i\,\hat{\mathbf{h}})\big)}{\hat{h}} + \mathcal{O}\big(\hat{h}^2\big) \tag{18}$$

In contrast to finite difference approximations, the complex-step method *is not* susceptible to subtraction error, and it can be used to compute derivatives accurate to round-off precision by setting an arbitrarily small imaginary step size (i.e., $\hat{h} \rightarrow 0$).

Once the CFD and the CAD sensitivities are computed, the gradient of the cost function follows from the application of the chain rule of differentiation

$$\nabla J = \frac{\partial J}{\partial \mathbf{X}_\mathrm{s}} \frac{\partial \mathbf{X}_\mathrm{s}}{\partial \boldsymbol{\alpha}} \tag{19}$$

2.5 Optimization Method. The optimization framework is driven by a gradient-based optimization algorithm that uses the values and gradients of the cost functions to update the design variables. Formally, this can be represented as

$$\boldsymbol{\alpha}^{k+1} = \mathcal{A}(\mathbf{J}(\boldsymbol{\alpha}^k),\, \nabla \mathbf{J}(\boldsymbol{\alpha}^k)) \tag{20}$$

where $\mathcal{A}(\cdot)$ stands for the algorithmic steps used by the optimizer at the kth iteration. The new set of design variables is used to update the CAD model, deform the mesh, and reevaluate the cost functions and gradients. This process is repeated until the optimization algorithm converges to an optimum solution. The optimizer adopted in this work is the sequential least squares programming algorithm [94] implemented in the SCIPY library [95], which is a sequential quadratic programing algorithm [17, pp. 526–572] capable to handle general nonlinear constraints as well as bounds for the design variables.

3 Validation of the Flow Solver

As documented by Vitale et al. [55], the RANS solver has already been validated against mass-averaged quantities and spanwise flow distributions measured in three different turbine configurations. In this section, the validation is complemented by comparing the blade surface pressure distributions predicted by the flow solver with the experimental data measured in three linear cascades:

1. The subsonic linear cascade measured by Kiock et al. [96] at DFVLR Braunschweig. This case is representative of a high-pressure turbine rotor, and it features a thick trailing edge typical of cooled blades.
2. The subsonic linear cascade measured by Hodson and Dominy [97] at the Whittle Laboratory. This case is representative of the root section of a high-lift, low-pressure turbine rotor.
3. The transonic linear cascade measured by Arts and Lambert de Rouvroit [98] at the Von Karman Institute for Fluid Dynamics. This case is representative of a high-pressure turbine stator that features a long semibladed region downstream the throat.

The boundary conditions that define each test case are summarized in Table 3. In all cases, the geometry of the blades was available as a list of point coordinates. To avoid the noise introduced

Table 3 Boundary conditions of the validation test cases

Reference	Fluid	α_{in} (deg)	$T_{0,\mathrm{in}}$ (K)	$p_{0,\mathrm{in}}$ (kPa)	p_{out} (kPa)	$I_{\mathrm{t,in}}$ (%)	$(\mu_{\mathrm{t}}/\mu)_{\mathrm{in}}$
Kiock et al. [96]	Air	30.0	313.0	63.8	41.9	0.50	10.0[a]
Hodson and Dominy [97]	Air	38.8	298.0[b]	41.4	29.8	0.50	10.0[a]
Arts and Lambert de Rouvroit [98]	Air	0.0	422.0	160.5	82.8	1.00	10.0[a]

[a] Assumed value. The solution has a weak dependence on this variable.

[b] The original publication indicates that the inlet temperature is close to ambient.

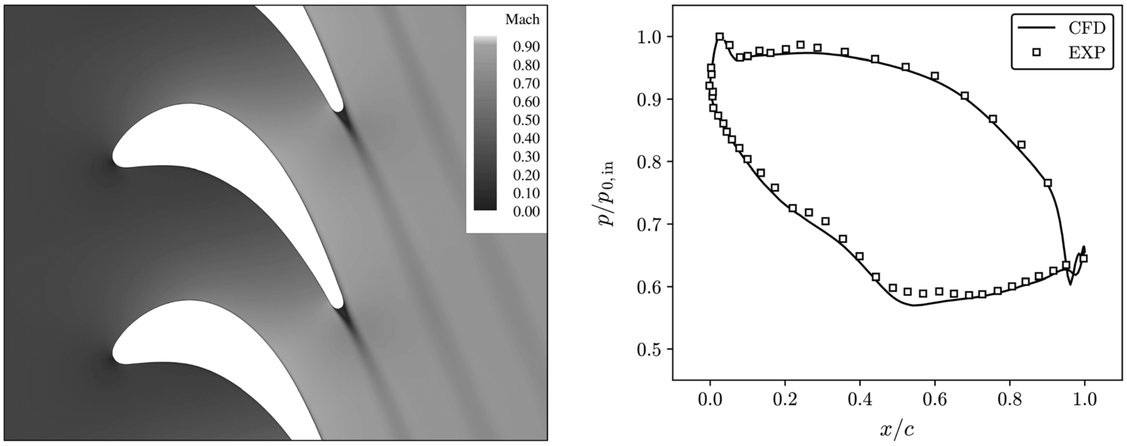

Fig. 3 Mach number contours (left) and surface pressure distribution (right) for the Kiock cascade [96]

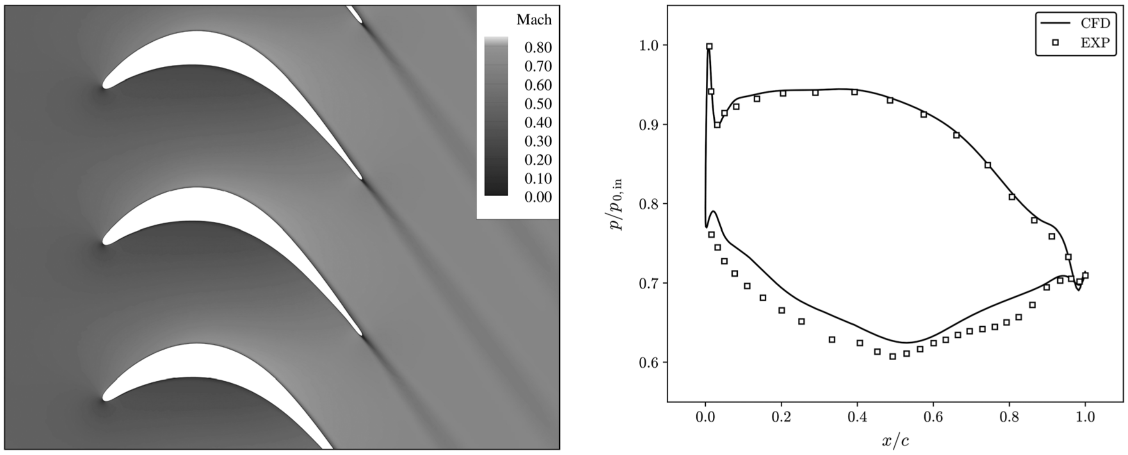

Fig. 4 Mach number contours (left) and surface pressure distribution (right) for the Hodson cascade [97]

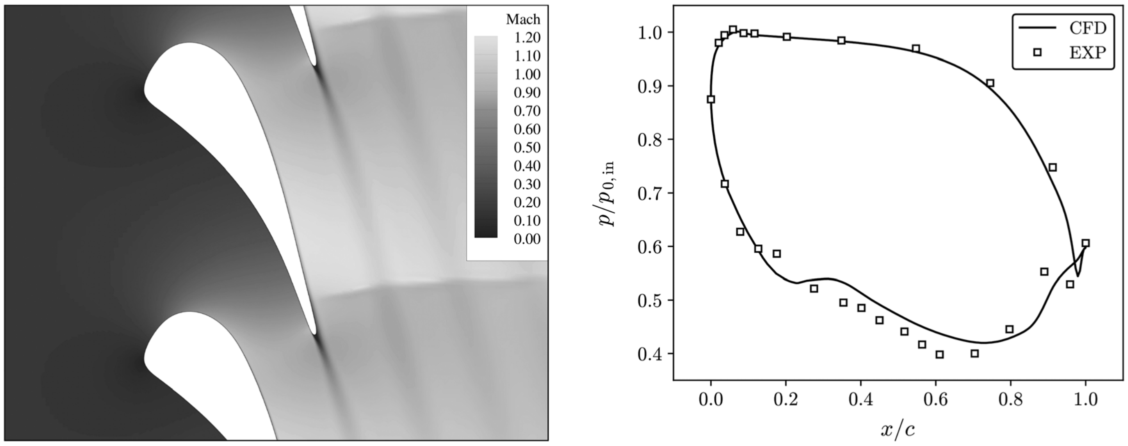

Fig. 5 Mach number contours (left) and surface pressure distribution (right) for the Arts cascade [98]

Table 4 Design specifications for the preliminary design

Variable	Symbol	Value	Unit
Working fluid		Isobutane	—
Inlet total temperature	$T_{0,\text{in}}$	125.0	°C
Inlet total pressure	$p_{0,\text{in}}$	400.0	kPa
Outlet static pressure	p_{out}	160.0	kPa
Mass flow rate	$\dot{m}$	1.600	kg/s
Angular speed	Ω	20,000	rpm
Radius at the hub	r_h	51.05	mm
Radius at the tip	r_t	63.75	mm
Axial chord	c_{ax}	10.00	mm
Axial spacing	s_{ax}	4.00	mm
Trailing edge thickness	t_{te}	0.50	mm
Degree of reaction	Λ	0.50	—

by coordinate round-off, the blade geometry was smoothed using the reparametrization methodology described in Ref. [58].

The flow solution in terms of Mach number and surface pressure distribution along fraction of true chord are shown in Figs. 3–5. The results show a good agreement between experimental data and the surface pressure distributions predicted by the flow solver for all three cases. As an additional check, the accuracy of the entropy generation prediction was evaluated for the Kiock cascade case. To this aim, the loss coefficient determined experimentally ($\zeta = 0.039$) was compared with simulation results ($\zeta = 0.043$), and the values obtained agreed reasonably well. Moreover, with regards to the Arts cascade case, the flow solver is able to predict the formation of a normal shock on the rear part of the blade suction side, which can be clearly seen in the Schlieren visualizations documented in Ref. [98]. These results supplement the validation reported in Ref. [55] and confirm that the RANS solver adopted is a suitable tool for the design and analysis of turbomachinery blades operating under subsonic and transonic conditions.

4 Application to a Case Study

The aerodynamic design method described above was applied to the design optimization of a single-stage turbine operating with isobutane (R600a) as working fluid. This turbine was specifically designed for experimental testing in the EXPAND facility at the Norwegian University of Science and Technology [60]. The fluid-dynamic design of the selected turbine was performed in two steps: a preliminary design phase in which the turbine layout and operating conditions are calculated, and an aerodynamic design phase in which the detailed shapes of the blades are defined and optimized.

4.1 Preliminary Design.

The preliminary turbine design was carried out using the mean-line model and optimization methodology documented in Ref. [99]. This method assumes that the flow is uniform along the spanwise and circumferential directions and solves the balance equations for mass and rothalpy at the inlet and outlet of each cascade, regardless of the detailed shape of the blades. In addition, the method uses the Kacker and Okapuu empirical loss model [100] to estimate the entropy generation in each blade row. More specifically, the original loss model was modified such that it takes into account the profile and trailing edge losses (2D effects) and neglects the tip-leakage and secondary losses (three-dimensional (3D) effects). This approach was adopted with the intent that the mean-line model used for the preliminary design and the two-dimensional RANS solver used for the aerodynamic design account for the same loss mechanisms.

The preliminary design was based on the specifications listed in Table 4, and it was performed using the total-to-total isentropic efficiency as objective function. This performance metric was adopted because it is an indication of the *blading efficiency* and it does not penalize the kinetic energy that is not recovered at the exhaust. The mass flow rate, inlet total temperature and pressure, outlet static pressure, hub and tip radii, and angular speed were the same as those of an existing turbine designed by an industrial partner. This design choice was adopted to ensure that the proposed turbine is compatible with the EXPAND facility. In addition, the axial chord of the stator and rotor blades was set to 10 mm ($H/c_{\text{ax}} = 1.27$) to obtain an aspect ratio above unity and limit the influence of secondary losses [101, p. 345], while the axial spacing was set to 4 mm ($s_{\text{ax}}/c_{\text{ax}} = 0.40$) to reduce the vibrational stresses induced in the rotor blades as they pass through the wakes of the stator blades [101, p. 333]. Furthermore, a trailing edge thickness of 0.50 mm was adopted due to manufacturing requirements.

As depicted in the cross-sectional view of Fig. 6, the proposed turbine is characterized by a constant annulus height and a relatively high hub-to-tip ratio ($r_\text{h}/r_\text{t} = 0.80$). Under these conditions, the radial variation of the flow is expected to be small [101, p. 204], and the use of a two-dimensional flow solver to carry out the detailed blade design is justified. Figure 6 also illustrates the *T*–*s* diagram of the expansion within the turbine. The expansion takes place in a thermodynamic region close to the vapor separation curve, and the fluid properties depart from ideal gas behavior ($Z_{\text{in}} \approx 0.95$). This highlights the importance of using an accurate thermodynamic model to carry out the fluid-dynamic design of the turbine. In addition, the velocity diagrams at the inlet and outlet of the rotor blades are illustrated in Fig. 7. Even if the degree of reaction Λ was set to 50%, the velocity triangles are not symmetrical because the axial velocity increases as the fluid expands to satisfy the mass conservation equation. The output of the

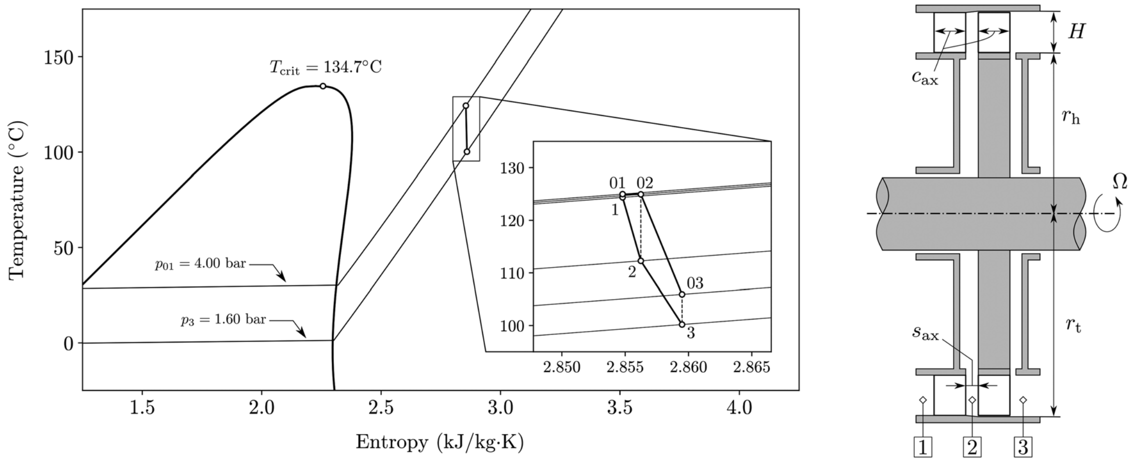

Fig. 6 ***T*–*s* diagram of the expansion (left) and schematic cross-sectional view of the turbine (right)**

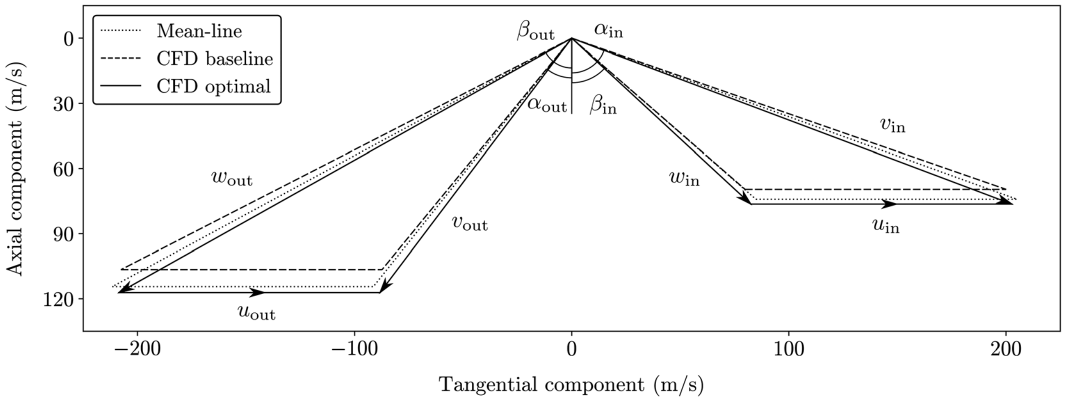

Fig. 7 Velocity triangles at the inlet and outlet of the rotor

Table 5 Boundary conditions for the aerodynamic design

Flow quantity	Symbol	Value	Unit
Inlet flow angle	α_{in}	0.0	deg
Inlet total temperature	$T_{0,\text{in}}$	125.0	°C
Inlet total pressure	$p_{0,\text{in}}$	400.0	kPa
Outlet static pressure	p_{out}	160.0	kPa
Inlet turbulence intensity	$I_{\text{turb,in}}$	1.00	%
Inlet viscosity ratio	$(\mu_t/\mu)_{\text{in}}$	10.0	—

Table 6 Thermophysical properties of isobutane (R600a)

Fluid property	Symbol	Value	Unit
Gas constant	R	143.1	J/kg K
Critical temperature	T_{crit}	407.8	K
Critical pressure	p_{crit}	3629	kPa
Acentric factor	ω	0.1835	—
Heat capacity ratio[a]	γ	1.086	—
Dynamic viscosity[a]	μ	9.918	μPa·s
Thermal conductivity[a]	k	28.8	mW/m K
Turbulence Prandtl number	Pr_t	0.90	—

[a] Evaluated at the inlet and assumed to be constant. All properties were obtained from the COOLPROP library [102–105].

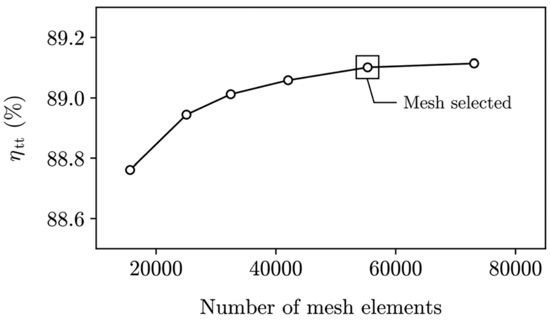

Fig. 9 Results of the mesh independence study in terms of total-to-total isentropic efficiency

preliminary design in terms of geometric parameters and operating conditions is reported in detail in the Appendix.

4.2 Aerodynamic Design

4.2.1 Baseline Turbine Configuration. The baseline geometry of the stator and rotor blades was defined using the CAD parametrization tool and then analyzed with the RANS flow solver. More specifically, the baseline stator and rotor blades were generated by trial-and-error with the aim to satisfy the velocity triangles obtained during the preliminary design phase. First, the blade axial chord and cascade spacing were specified, and a tentative

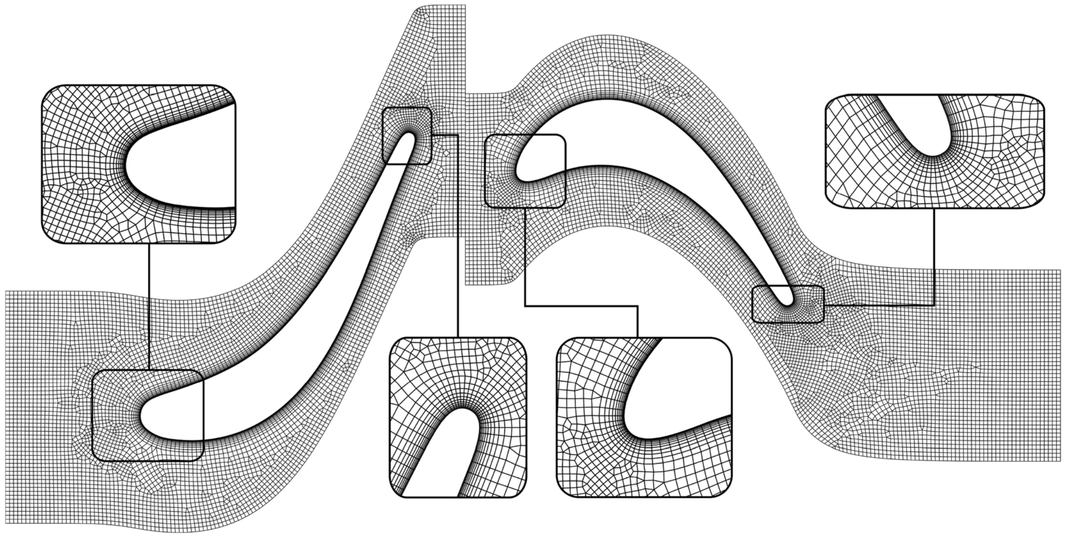

Fig. 8 Computational grid of the baseline geometry with a close-up view of the inflation layers

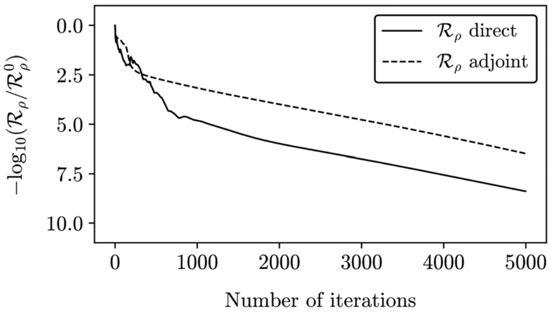

Fig. 10 Convergence history of the direct and adjoint solvers for the baseline rotor flow domain

camber-line was defined using the metal and stagger angles obtained from the mean-line model. After that, a preliminary thickness distribution was imposed in the direction normal to the camber-line. This thickness distribution was defined in an iterative way aiming to achieve smooth blade surfaces as well as a continuous decrease of passage area from the inlet of the cascade to the throat. Finally, the stagger angle and the trailing edge thickness distribution were carefully adjusted to achieve a throat opening yielding a gauging angle (i.e., $\cos\beta_g = o/s$) close to the exit flow angle obtained from the mean-line design.

The boundary conditions used for the flow simulations are summarized in Table 5, and the parameters used to describe the thermophysical behavior of the fluid are summarized in Table 6. As depicted in Fig. 8, the flow domain was discretized using an unstructured grid, and the number of mesh elements was selected in accordance with the results of the mesh independence study shown in Fig. 9. In addition, the size of the cells in the direction normal to the blade walls was controlled with inflation layers to ensure that the boundary layer is resolved accurately ($y^+ < 1$). The direct and adjoint problems were driven to steady-state using a Courant–Friedrichs–Lewy number of 25, and the termination criterion was set to 5000 iterations, which corresponds to a residual reduction of about 9 and 8 orders of magnitude, respectively. The convergence history of the direct and adjoint solvers is shown in Fig. 10. As expected from the duality-preserving property of the adjoint formulation, both solvers essentially exhibit the same convergence rate.

The flow field around the baseline geometry is illustrated in Fig. 11, and it is characterized by the presence of a shock wave pattern at the trailing edge of each row of blades. Both cascades operate at transonic conditions, and the highest relative Mach numbers within the stator and rotor flow passage are 1.48 and

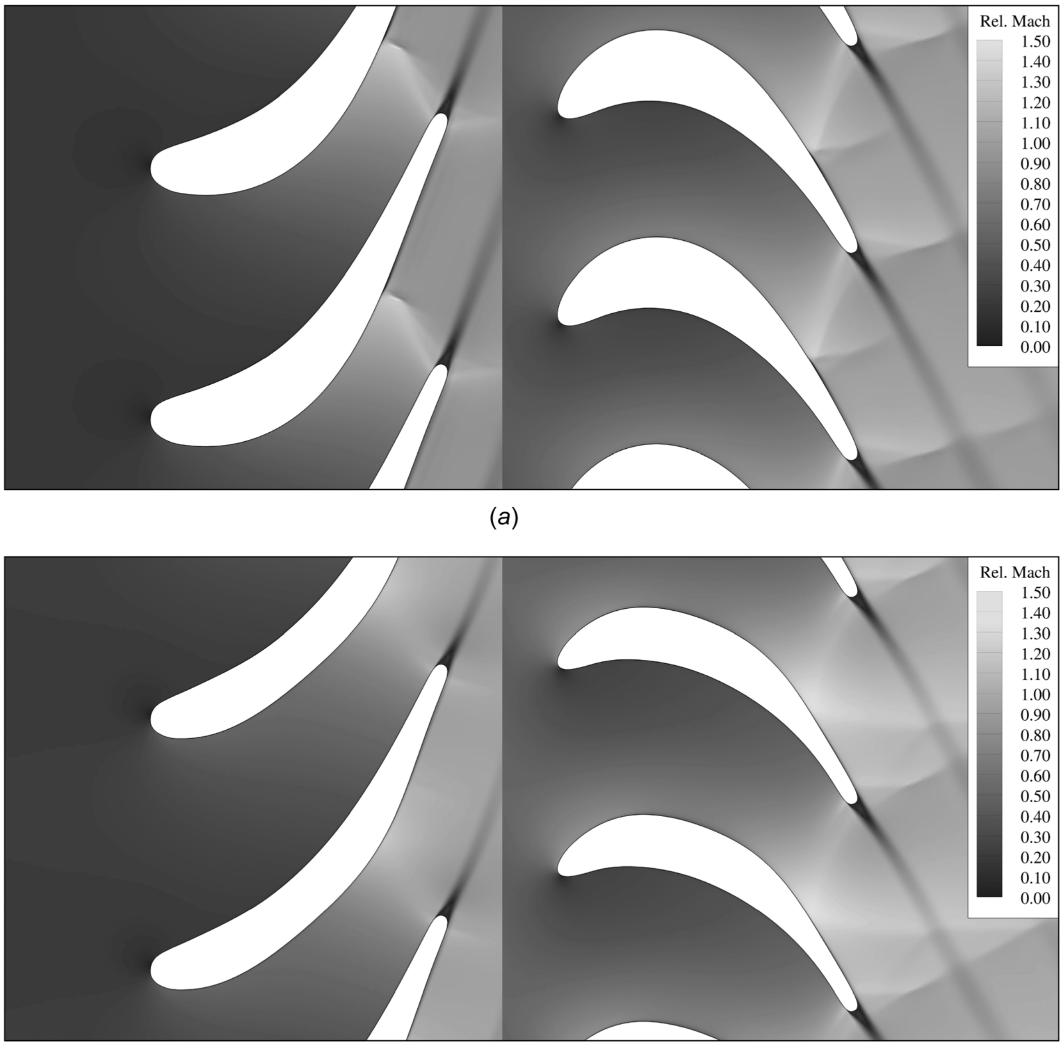

(*a*)

(*b*)

Fig. 11 (*a*) Relative Mach number contours of the flow field for the baseline design and (*b*) relative Mach number contours of the flow field for the optimal design

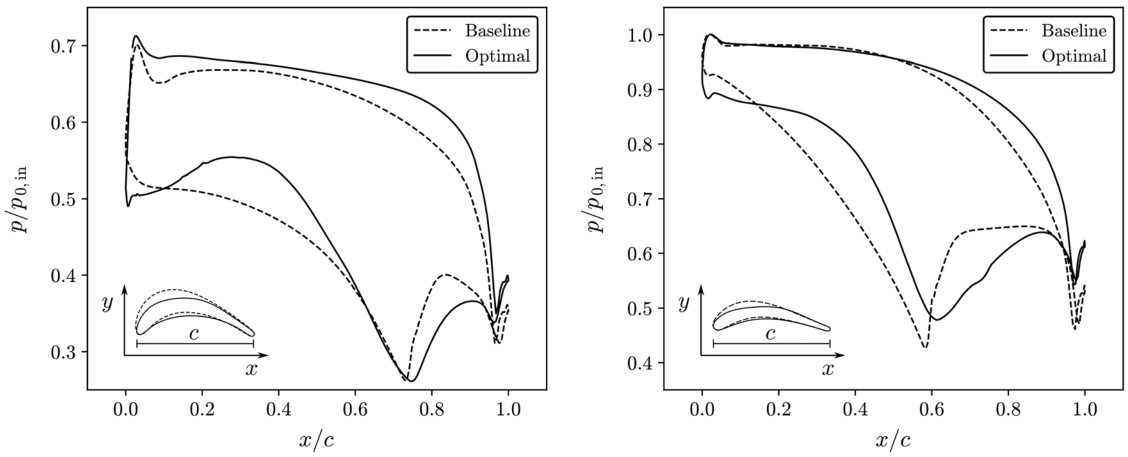

Fig. 12 Surface pressure distribution over the stator (left) and rotor (right) blades

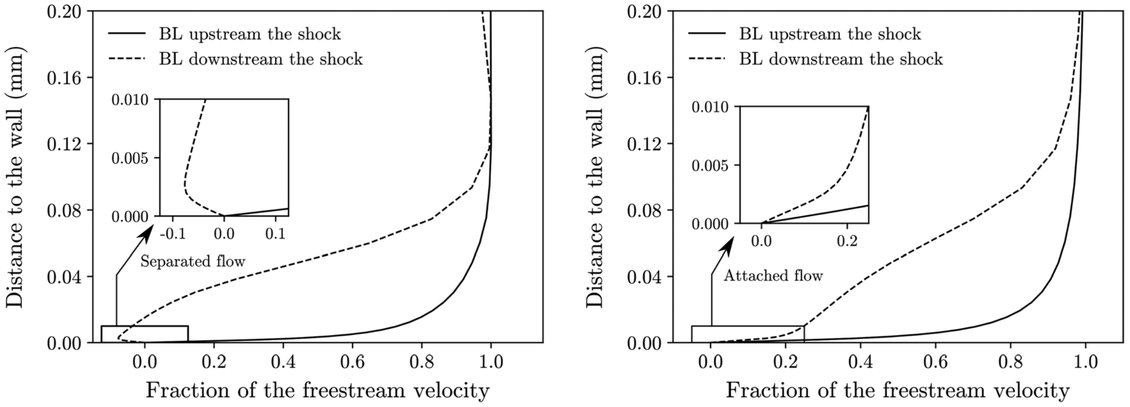

Fig. 13 Boundary layers upstream and downstream the shock for the stator (left) and rotor blades (right)

1.38, respectively. The stator surface pressure distribution, see Fig. 12 (left), indicates that the flow accelerates over the entire pressure side and also over the suction side until $x/c \approx 0.58$. At this location, the shock wave originating at the trailing edge of the adjacent stator blade impinges on the suction side, causing a steep increase of the surface pressure. This adverse pressure gradient leads to the formation of a small separation bubble in the region downstream of the impingement. This is illustrated in Fig. 13 (left), where a negative-velocity region can be identified in the proximity of the blade surface. The flow over the rotor blades is similar, but, in this case, the shock wave impinging on the rotor suction side at $x/c \approx 0.73$ is weaker and does not cause flow separation. Instead, the boundary layer remains attached and becomes thicker after the interaction with the shock wave, see Fig. 13 (right).

4.2.2 Optimized Turbine Configuration. The proposed aerodynamic shape optimization framework was utilized to minimize the entropy generation arising from viscous dissipation and shock waves [106]. To this aim, the shape of the baseline stator and rotor blades was simultaneously optimized using the CAD model parameters listed in Table 2 as design variables. The blade spacing, axial chord, and stagger angle were kept constant to maintain the same number of blades and axial length, resulting in a total of 36 degrees-of-freedom (18 per blade). In addition, the minimum thickness was constrained to 0.50 mm to satisfy the manufacturing requirements. Other typical aerodynamic constraints such as the mass flow rate, power output, or total-to-total pressure ratio were not included in the optimization because the turbine considered is specifically designed for experimental testing in a flexible research facility that does not impose limitations on the values of these variables.

The accuracy of the objective function gradient was verified prior to the optimization. Figure 14 shows a comparison of the entropy generation gradient computed using Eq. (19) against that computed by applying forward finite differences to the entire evaluation chain. The step size used for the forward finite differences was 1%. The results indicate an excellent agreement between the adjoint-based and finite difference gradients, confirming that the CAD model and the CFD solver are correctly differentiated. In addition, these results demonstrate the superiority of the adjoint-based approach, which only required one direct and one adjoint problem solutions to evaluate the gradient. In contrast, the finite

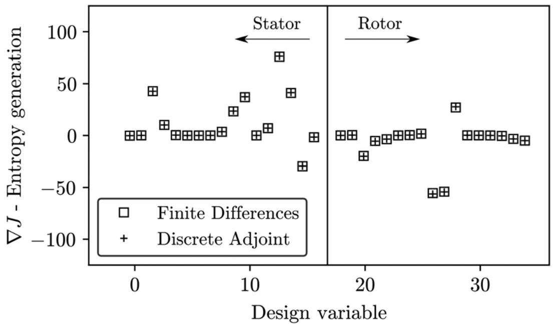

Fig. 14 Verification of the cost function adjoint-based sensitivities against forward finite differences

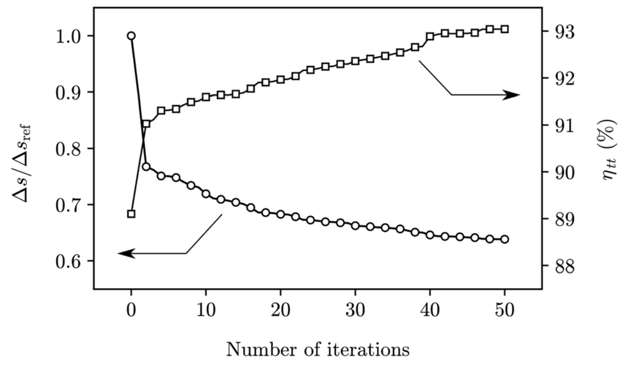

Fig. 15 Optimization convergence history in terms of entropy generation and total-to-total efficiency

difference gradient evaluation required $36+1$ direct problem solutions, one for the baseline and one per perturbed design variable.

The convergence history of the optimization problem is shown in Fig. 15. The optimization was stopped after 50 design cycles because the improvement of the objective function value was marginal. The total run-time was approximately 60 h on a six-core computer with a CPU rate of 2.2 GHz. The entropy generation was reduced by 36.2% relative to that of the baseline configuration, which corresponds to a total-to-total isentropic efficiency increase from 89.10% to 93.04%. The large majority of the objective function improvement took place in the first ten design steps.

The flow field around the optimal geometry is illustrated in Fig. 11. It can be observed that the optimizer reduced the curvature of the blades, especially on the suction side, and that the minimum thickness constraint was respected. The changes in curvature reduced the maximum Mach number in the stator cascade from 1.48 to 1.17. As a result, the trailing edge shock pattern, as well as the separation bubble caused by the shock-boundary layer interaction, was eliminated. Conversely, in the rotor flow passage, the maximum relative Mach number decreased from 1.38 to 1.35. Despite the small reduction in peak Mach number, the surface pressure distribution depicted in Fig. 12 (right) indicates that the shock impinging on the rotor suction side is significantly weaker for the optimal geometry. As a result, the boundary layer downstream of the impinging shock is thinner and more stable than for the baseline geometry, see Fig. 16. In addition, the optimizer also reduced the entropy generation due to mixing downstream of the blades. This can be inferred by inspecting the entropy distributions shown in Fig. 17. The cumulative entropy value, computed by spatially integrating the entropy distribution over the pitch, was reduced by 40.4% for the case of the stator and by 25.0% for the case of the rotor. This is a remarkable improvement given that the trailing edge thickness, which has a strong influence on the entropy generation downstream of the blades [106], was not reduced during the optimization.

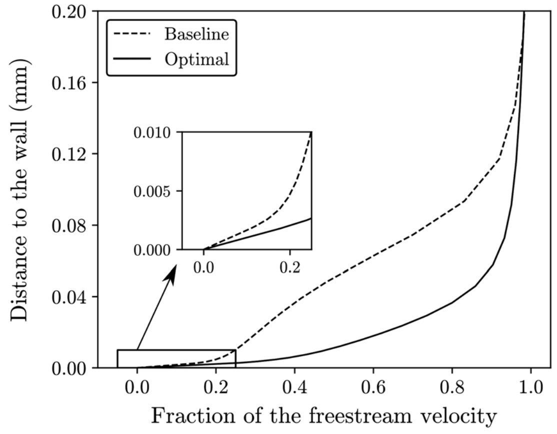

Fig. 16 Rotor boundary layer downstream the shock for the baseline and optimal geometries

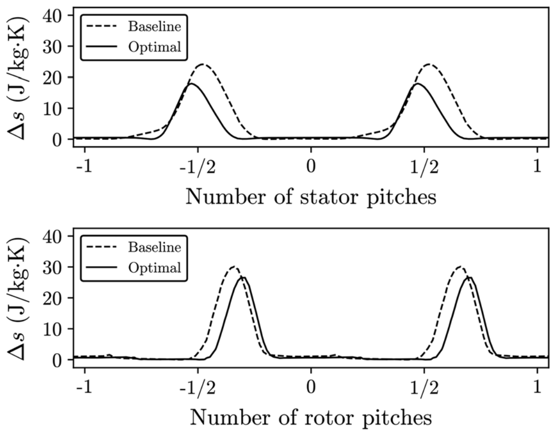

Fig. 17 Pitchwise entropy distribution in the planes located at a distance $x = 0.2\,c_{\mathrm{ax}}$ downstream of the stator and rotor trailing edges

5 Conclusions

An aerodynamic design method for turbomachines operating in the nonideal compressible flow regime was developed and documented in this paper. The method relies on a new gradient-based shape optimization framework that integrates a differentiated CAD-based parametrization method with a multirow turbomachinery RANS solver capable to treat nonideal flows and its discrete adjoint counterpart. The proposed method was applied to the design optimization of a single-stage axial turbine utilizing isobutane (R600a) as working fluid to demonstrate its capability. The following conclusions were drawn from the results of this study:

(1) The accuracy of the objective function gradients obtained from the adjoint-based shape optimization framework was verified against forward finite differences. The results showed an excellent agreement between the two methods, confirming that the parametric CAD model and the RANS solver are correctly differentiated.
(2) The CAD-based parametrization enabled the definition of high-level geometric constraints such as constant axial chord length, minimum trailing edge thickness, and smooth curvature distribution in a straightforward way. This is a significant advantage over mesh-based methods, which are not well-suited to impose geometric constraints.
(3) The optimization framework was successfully applied to design unconventional blade shapes that minimize the entropy generation arising from viscous dissipation and shock waves. In particular, the optimizer reduced the entropy generation by 36.2% relative to the baseline geometry in 50 design cycles, which corresponds to a total-to-total isentropic efficiency increase of 3.94 percentage points.
(4) The aerodynamic design optimization did not only produce a quantitative improvement in performance but also caused qualitative changes in the flow field. Most notably, the baseline stator cascade featured a trailing edge shock pattern and a shock-induced separation bubble at the suction side that were eliminated as a result of the optimization.

Future work will be devoted to the extension of the shape optimization framework to handle three-dimensional problems as well as to account for the influence of other disciplines, such as stress analysis and aero-elasticity. In addition, the turbine designed in this paper will be manufactured and tested in the EXPAND facility [60] at the Norwegian University of Science and Technology with the aim to provide experimental datasets concerning turbines operating with organic working fluids. The authors would like to mention that the shape optimization framework proposed in this paper was released under an open-source license, and it is available in an online repository [61].

Acknowledgment

The authors gratefully acknowledge the financial support from the Research Council of Norway (EnergiX Grant No. 255016) for the COPRO project, the Netherlands Organization for Scientific Research (Grant Project No. 14711), and the user partners Equinor, Hydro, Alcoa, GE Power Norway, and FrioNordica. The authors would also like to thank ENOGIA for providing the reference data for the preliminary turbine design.

Funding Data

- Research Council of Norway (EnergiX Grant No. 255016; Funder ID: 10.13039/501100005416).
- Netherlands Organization for Scientific Research (Grant Project No. 14711; Funder ID: 10.13039/501100003246).
- User partners Equinor, Hydro, Alcoa, GE Power Norway, and FrioNordica.

Nomenclature

Latin Letters

a = speed of sound (m/s)
c = blade chord (m)
c_{ax} = blade axial chord (m)
d_{in} = blade leading edge tangent proportion
d_{out} = blade trailing edge tangent proportion
e = static specific energy (J/kg)
E = stagnation specific energy (J/kg)
$\mathbf{F}^{\mathrm{c}}$ = vector of convective fluxes (several)
$\mathbf{F}^{\mathrm{v}}$ = vector of viscous fluxes (several)
$\mathbf{G}$ = RANS system fixed-point operator (several)
h = static specific enthalpy (J/kg)
H = blade height (m)
$\hat{h}$ = complex step size (several)
h_0 = stagnation specific enthalpy (J/kg)
$\mathbf{I}$ = identity matrix
I_{t} = turbulence intensity
J = cost function
$\mathbf{J}$ = vector of cost functions
k = molecular thermal conductivity (W/m K)
k_{t} = turbulence thermal conductivity (W/m K)
L = Lagrangian function
$\mathbf{M}$ = mesh deformation operator (several)
$\dot{m}$ = mass flow rate (kg/s)
Ma = Mach number
$\mathbf{N}$ = adjoint system fixed-point operator (several)
N_{b} = number of blades
o = blade opening (m)
p = static pressure (Pa)
$\mathbf{P}$ = RANS preconditioning matrix (several)
p_0 = stagnation pressure (Pa)
$\dot{\mathbf{q}}$ = heat flux vector (W/m^2)
R = gas constant (J/kg K)
$\mathbf{R}$ = numerical residual vector (several)
r_{h} = turbine radius at the hub (m)
r_{in} = blade leading edge radius of curvature (m)
r_{out} = blade trailing edge radius of curvature (m)
r_{t} = turbine radius at the tip (m)
s = specific entropy of blade spacing (J/kg K or m)
$\mathbf{S}$ = source term vector (several)
s_{ax} = axial spacing between stator and rotor (m)
T = static temperature (K)
t_{te} = blade trailing edge thickness (m)
T_0 = stagnation temperature (K)
t^{l} = blade lower thickness distribution (m)
t^{u} = blade upper thickness distribution (m)
u = blade velocity magnitude (m/s)
$\mathbf{U}$ = flow solution (several)
v = absolute flow velocity magnitude (m/s)
$\mathbf{v}$ = absolute flow velocity vector (m/s)
w = relative flow velocity magnitude (m/s)
$\mathbf{w}$ = relative flow velocity vector (m/s)
$\dot{W}$ = power output (W)
$\mathbf{X}$ = position vector (m)
$\mathbf{X}_{\mathrm{s}}$ = boundary mesh coordinates (m)
$\mathbf{X}_{\mathrm{v}}$ = interior mesh coordinates (m)
Y = pressure loss coefficient, $Y = (p_{0\mathrm{rel,in}} - p_{0\mathrm{rel,out}})/(p_{0\mathrm{rel,out}} - p_{\mathrm{out}})$
y^+ = nondimensional wall distance
Z = compressibility factor, $Z = p/\rho RT$
ΔS = area of a control volume face (m^2)
Δt = time-step (s)
ΔV = volume of a control volume cell (m^3)

Greek Symbols

α = absolute flow angle (deg)
$\boldsymbol{\alpha}$ = set of design variables (several)
β = relative flow angle (deg)
β_{g} = gauging angle, $\cos\beta_{\mathrm{g}} = o/s$ (deg)
γ = heat capacity ratio
δ_{ij} = Kronecker delta function
ζ = energy loss coefficient, $\zeta = (h_{\mathrm{out}} - h_{\mathrm{out,s}})/(h_{0,\mathrm{in}} - h_{\mathrm{out,s}})$
η_{ts} = total-to-static efficiency, $\eta_{\mathrm{ts}} = (h_{01} - h_{03})/(h_{01} - h_{03s})$
η_{tt} = total-to-total efficiency, $\eta_{\mathrm{tt}} = (h_{01} - h_{03})/(h_{01} - h_{3s})$
θ_{in} = blade leading edge metal angle (deg)
θ_{out} = blade trailing edge metal angle (deg)
$\boldsymbol{\lambda}$ = Lagrange multipliers (several)
Λ = degree of reaction, $\Lambda = (h_2 - h_3)/(h_1 - h_3)$
μ = molecular dynamic viscosity (Pa·s)
$\boldsymbol{\mu}$ = Lagrange multipliers (several)
μ_{t} = turbulence dynamic viscosity (Pa·s)
ξ = blade stagger angle (deg)
ρ = density (kg/m^3)
$\boldsymbol{\tau}$ = shear stress tensor (Pa)
ω = acentric factor
Ω = angular speed magnitude (rpm)
$\boldsymbol{\Omega}$ = angular speed vector (rpm)

Subscripts and Superscripts

crit = critical point
in = inlet or leading edge
out = outlet or trailing edge
rel = relative frame of reference
s = isentropic state
0 = stagnation state
1 = flow station upstream the stator
2 = flow station between stator and rotor
3 = flow station downstream the rotor

Appendix

Table 7 summarizes the main geometric parameters and operating conditions obtained from the preliminary and aerodynamic design phases. The variables reported only at index (1) refer to the turbine as a whole, whereas those reported at indices (1,2) refer to the stator and rotor rows, and those reported at indices (1,2,3) refer to the flow stations indicated in Fig. 6. The operating conditions of the *baseline geometry* and *optimal geometry* columns were computed from area-averaged quantities obtained by post-processing the CFD solution.

Table 7 Geometry and operating conditions obtained from the preliminary and aerodynamic design phases

		Mean-line model			Aerodynamic baseline			Aerodynamic optimal		
Variable	Unit	1	2	3	1	2	3	1	2	3
Ω	rpm	20,000	—	—	20,000	—	—	20,000	—	—
$\dot{m}$	kg/s	1.600	—	—	1.507	—	—	1.660	—	—
$\dot{W}$	kW	57.02	—	—	52.58	—	—	58.41	—	—
η_{ts}	%	72.75	—	—	71.66	—	—	72.44	—	—
η_{tt}	%	93.11	—	—	89.10	—	—	93.04	—	—
Λ	—	0.500	—	—	0.493	—	—	0.492	—	—
Y	—	0.061	0.072	—	0.124	0.118	—	0.066	0.089	—
N_b	—	42	51	—	42	51	—	42	51	—
c	mm	12.20	10.06	—	14.32	10.98	—	14.32	10.98	—
c_{ax}	mm	10.00	10.00	—	10.00	10.00	—	10.00	10.00	—
s	mm	8.59	7.07	—	8.59	7.07	—	8.59	7.07	—
o	mm	2.92	3.36	—	2.95	3.34	—	3.16	3.57	—
t_{te}	mm	0.50	0.50	—	0.50	0.50	—	0.50	0.50	—
r_h	mm	51.05	51.05	51.05	51.05	51.05	51.05	51.05	51.05	51.05
r_t	mm	63.75	63.75	63.75	63.75	63.75	63.75	63.75	63.75	63.75
p	kPa	391.4	252.4	160.0	392.4	251.5	159.9	390.8	252.2	159.9
T	°C	124.4	112.5	100.6	124.4	111.0	97.9	124.2	110.4	97.0
a	m/s	238.2	237.4	235.8	238.9	237.6	235.5	238.9	237.4	235.2
Z	—	0.959	0.971	0.980	0.955	0.968	0.978	0.955	0.968	0.978
Ma	—	0.204	0.918	0.621	0.191	0.892	0.585	0.211	0.913	0.624
Ma_{rel}	—	0.204	0.475	1.020	0.191	0.446	0.991	0.211	0.474	1.017
α	deg	0.00	70.12	−38.62	0.00	70.82	−39.35	0.00	69.35	−37.01
β	deg	0.00	48.83	−61.61	0.00	48.92	−62.83	0.00	47.19	−60.67

References

[1] Van den Braembussche, R. A., 2008, "Numerical Optimization for Advanced Turbomachinery Design," *Optimization and Computational Fluid Dynamics*, D. Thévenin and G. Janiga, eds., Springer/Berlin, Germany, pp. 147–189.

[2] Denton, J. D., 2010, "Some Limitations of Turbomachinery CFD," ASME Paper No. GT2010-22540.

[3] Kluwick, A., 2017, "Non-Ideal Compressible Fluid Dynamics: A Challenge for Theory," J. Phys.: Conf. Ser., **821**, p. 012001.

[4] Colonna, P., Harinck, J., Rebay, S., and Guardone, A., 2008, "Real-Gas Effects in Organic Rankine Cycle Turbine Nozzles," J. Propul. Power, **24**(2), pp. 282–294.

[5] Pasquale, D., Ghidoni, A., and Rebay, S., 2013, "Shape Optimization of an Organic Rankine Cycle Radial Turbine Nozzle," ASME J. Eng. Gas Turbines Power, **135**(4), p. 042308.

[6] Persico, G., Rodriguez-Fernandez, P., and Romei, A., 2019, "High-Fidelity Shape Optimization of Non-Conventional Turbomachinery by Surrogate Evolutionary Strategies," ASME J. Turbomach., **141**(8), p. 081010.

[7] Baltadjiev, N. D., Lettieri, C., and Spakovszky, Z. S., 2015, "An Investigation of Real Gas Effects in Supercritical CO_2 Centrifugal Compressors," ASME J. Turbomach., **137**(9), p. 091003.

[8] Romei, A., Gaetani, P., Giostri, A., and Persico, G., 2020, "The Role of Turbomachinery Performance in the Optimization of Supercritical Carbon Dioxide Power Systems," ASME J. Turbomach., **142**(7), p. 071001.

[9] Mounier, V., Picard, C., and Schiffmann, J., 2018, "Data-Driven Predesign Tool for Small-Scale Centrifugal Compressor in Refrigeration," ASME J. Eng. Gas Turbines Power, **140**(12), p. 121011.

[10] Meroni, A., Graa, J., Persico, G., and Haglind, F., 2018, "Optimization of Organic Rankine Cycle Power Systems Considering Multistage Axial Turbine Design," Appl. Energy, **209**, pp. 339–354.

[11] Audet, C., and Hare, W., 2017, *Derivative-Free and Blackbox Optimization*, 1st ed., Springer, Cham, Switzerland.

[12] Mueller, L., Alsalihi, Z., and Verstraete, T., 2013, "Multidisciplinary Optimization of a Turbocharger Radial Turbine," ASME J. Turbomach., **135**(2), p. 021022.

[13] De Servi, C. M., Burigana, M., Pini, M., and Colonna, P., 2019, "Design Method and Performance Prediction for Radial-Inflow Turbines of High-Temperature Mini-Organic Rankine Cycle Power Systems," ASME J. Eng. Gas Turbines Power, **141**(9), p. 091021.

[14] Oyama, A., Liou, M.-S., and Obayashi, S., 2004, "Transonic Axial-Flow Blade Optimization: Evolutionary Algorithms/Three-Dimensional Navier-Stokes Solver," J. Propul. Power, **20**(4), pp. 612–619.

[15] Samad, A., Kim, K.-Y., Goel, T., Haftka, R. T., and Shyy, W., 2008, "Multiple Surrogate Modeling for Axial Compressor Blade Shape Optimization," J. Propul. Power, **24**(2), pp. 301–310.

[16] Verstraete, T., 2019, "Toward Gradient-Based Optimization of Full Gas Turbines," ASME Mech. Eng., **141**(3), pp. 54–55.

[17] Nocedal, J., and Wright, S. J., 2006, *Numerical Optimization*, 2nd ed., Springer, New York.

[18] Giles, M. B., and Pierce, N. A., 2000, "An Introduction to the Adjoint Approach to Design," Flow, Turbul. Combust., **65**(3/4), pp. 393–415.

[19] Peter, J. E. V., and Dwight, R. P., 2010, "Numerical Sensitivity Analysis for Aerodynamic Optimization: A Survey of Approaches," Comput. Fluids, **39**(3), pp. 373–391.

[20] Pironneau, O., 1974, "On Optimum Design in Fluid Mechanics," J. Fluid Mech., **64**(1), pp. 97–110.

[21] Jameson, A., 1988, "Aerodynamic Design Via Control Theory," J. Sci. Comput., **3**(3), pp. 233–260.

[22] Jameson, A., 1995, "Optimum Aerodynamic Design Using CFD and Control Theory," AIAA Paper No. 95-1729.

[23] Reuther, J., Jameson, A., Farmer, J., Martinelli, L., and Saunders, D., 1996, "Aerodynamic Shape Optimization of Complex Aircraft Configurations Via an Adjoint Formulation," AIAA Paper No. 96-0094.

[24] Yang, S., Wu, H.-Y., Liu, F., and Tsai, H.-M., 2003, "Optimum Aerodynamic Design of Cascades by Using an Adjoint Equation Method," AIAA Paper No. 2003-1068.

[25] Wu, H.-Y., Yang, S., Liu, F., and Tsai, H.-M., 2003, "Comparisons of Three Geometric Representations of Airfoils for Aerodynamic Optimization," AIAA Paper No. 2003-4095.

[26] Wu, H.-Y., Liu, F., and Tsai, H.-M., 2005, "Aerodynamic Design of Turbine Blades Using an Adjoint Equation Method," AIAA Paper No. 2005-1006.

[27] Arens, K., Rentrop, P., Stoll, S., and Wever, U., 2005, "An Adjoint Approach to Otimal Design of Turbine Blades," Appl. Numer. Math., **53**(2–4), pp. 93–105.

[28] Li, Y., Yang, D., and Feng, Z., 2006, "Inverse Problem in Aerodynamic Shape Design of Turbomachinery Blades," ASME Paper No. GT2006-91135.

[29] Papadimitriou, D. I., and Giannakoglou, K. C., 2006, "Compressor Blade Optimization Using a Continuous Adjoint Formulation," ASME Paper No. GT2006-90466.

[30] Duta, M. C., Shahpar, S., and Giles, M. B., 2007, "Turbomachinery Design Optimization Using Automatic Differentiated Adjoint Code," ASME Paper No. GT2007-28329.

[31] Corral, R., and Gisbert, F., 2008, "Profiled End Wall Design Using an Adjoint Navier–Stokes Solver," ASME J. Turbomach., **130**(2), p. 021011.

[32] Wang, D. X., and He, L., 2010, "Adjoint Aerodynamic Design Optimization for Blades in Multistage Turbomachines—Part I: Methodology and Verification," ASME J. Turbomach., **132**(2), p. 021011.

[33] Wang, D. X., He, L., Li, Y. S., and Wells, R. G., 2010, "Adjoint Aerodynamic Design Optimization for Blades in Multistage Turbomachines—Part II: Validation and Application," ASME J. Turbomach., **132**(2), p. 021012.

[34] Luo, J., Xiong, J., Liu, F., and McBean, I., 2011, "Three-Dimensional Aerodynamic Design Optimization of a Turbine Blade by Using an Adjoint Method," ASME J. Turbomach., **133**(1), p. 011026.

[35] Walther, B., and Nadarajah, S., 2013, "Constrained Adjoint-Based Aerodynamic Shape Optimization of a Single-Stage Transonic Compressor," ASME J. Turbomach., **135**(2), p. 021017.

[36] Luo, J., Zhou, C., and Liu, F., 2014, "Multipoint Design Optimization of a Transonic Compressor Blade by Using an Adjoint Method," ASME J. Turbomach., **136**(5), p. 051005.

[37] Walther, B., and Nadarajah, S., 2014, "An Adjoint-Based Optimization Method for Constrained Aerodynamic Shape Design of Three-Dimensional Blades in Multi-Row Turbomachinery Configurations," ASME Paper No. GT2014-26604.

[38] Pini, M., Persico, G., Pasquale, D., and Rebay, S., 2015, “Adjoint Method for Shape Optimization in Real-Gas Flow Applications,” ASME J. Eng. Gas Turbines Power, **137**(3), p. 032604.
[39] Xu, S., Radford, D., Meyer, M., and Müller, J.-D., 2015, “CAD-Based Adjoint Shape Optimisation of a One-Stage Turbine With Geometric Constraints,” ASME Paper No. GT2015-42237.
[40] Montanelli, H., Montagnac, M., and Gallard, F., 2015, “Gradient Span Analysis Method: Application to the Multipoint Aerodynamic Shape Optimization of a Turbine Cascade,” ASME J. Turbomach., **137**(9), p. 091006.
[41] Luo, J., Liu, F., and McBean, I., 2015, “Turbine Blade Row Optimization Through Endwall Contouring by an Adjoint Method,” J. Propul. Power, **31**(2), pp. 505–518.
[42] Walther, B., and Nadarajah, S., 2015, “Adjoint-Based Constrained Aerodynamic Shape Optimization for Multistage Turbomachines,” J. Propul. Power, **31**(5), pp. 1298–1319.
[43] Walther, B., and Nadarajah, S., 2015, “Optimum Shape Design for Multirow Turbomachinery Configurations Using a Discrete Adjoint Approach and an Efficient Radial Basis Function Deformation Scheme for Complex Multiblock Grids,” ASME J. Turbomach., **137**(8), p. 081006.
[44] Walther, B., and Nadarajah, S., 2015, “An Adjoint-Based Multi-Point Optimization Method for Robust Turbomachinery Design,” ASME Paper No. GT2015-44142.
[45] Tang, X., Luo, J., and Liu, F., 2018, “Adjoint Aerodynamic Optimization of a Transonic Fan Rotor Blade With a Localized Two-Level Mesh Deformation Method,” Aerosp. Sci. Technol., **72**, pp. 267–277.
[46] Mueller, L., and Verstraete, T., 2017, “CAD Integrated Multipoint Adjoint-Based Optimization of a Turbocharger Radial Turbine,” Int. J. Turbomach., Propul. Power, **2**(3), p. 14.
[47] Vitale, S., Albring, T. A., Pini, M., Gauger, N. R., and Colonna, P., 2017, “Fully Turbulent Discrete Adjoint Solver for Non-Ideal Compressible Flow Applications,” J. Global Power Propul. Soc., **1**, pp. 252–270.
[48] Luers, M., Sagebaum, M., Mann, S., Backhaus, J., Grossmann, D., and Gauger, N. R., 2018, “Adjoint-Based Volumetric Shape Optimization of Turbine Blades,” AIAA Paper No. 2018-3638.
[49] Anand, N., Vitale, S., Pini, M., and Colonna, P., 2018, “Assessment of FFD and CAD-Based Shape Parametrization Methods for Adjoint-Based Turbomachinery Shape Optimization,” Proceedings of the Montreal 2018 Global Power and Propulsion Forum, Montreal, QC, Canada, May 7–9, pp. 1–8.
[50] Mykhaskiv, O., Banović, M., Auriemma, S., Mohanamuraly, P., Walther, A., Legrand, H., and Müller, J.-D., 2018, “NURBS-Based and Parametric-Based Shape Optimization With Differentiated CAD Kernel,” Comput.-Aided Des. Appl., **15**(6), pp. 916–926.
[51] Sanchez Torreguitart, I., Verstraete, T., and Mueller, L., 2018, “Optimization of the LS89 Axial Turbine Profile Using a CAD and Adjoint Based Approach,” Int. J. Turbomach., Propul. Power, **3**(3), p. 20.
[52] Sanchez Torreguitart, I., Verstraete, T., and Mueller, L., 2019, “CAD and Adjoint Based Multipoint Optimization of an Axial Turbine Profile,” *Evolutionary and Deterministic Methods for Design Optimization and Control With Applications to Industrial and Societal Problems*, E. Andrés-Pérez, L. M. González, J. Periaux, N. Gauger, D. Quagliarella, and K. Giannakoglou, eds., Springer International Publishing, Cham, Switzerland, pp. 35–46.
[53] Russo, V., Orsenigo, S., Mueller, L., Verstraete, T., and Lavagnoli, S., 2019, “Adjoint Based Aerodynamic Optimization of a Multi-Splitter Turbine Vane Frame,” ASME Paper No. GT2019-91608.
[54] Rubino, A., Vitale, S., Colonna, P., and Pini, M., 2020, “Fully-Turbulent Adjoint Method for the Unsteady Shape Optimization of Multi-Row Turbomachinery,” Aerosp. Sci. Technol., **106**, p. 106132.
[55] Vitale, S., Pini, M., and Colonna, P., 2020, “Multistage Turbomachinery Design Using the Discrete Adjoint Method Within the Open-Source Software SU2,” J. Propul. Power, **36**(3), pp. 465–478.
[56] Samareh, J. A., 2001, “Survey of Shape Parameterization Techniques for High-Fidelity Multidisciplinary Shape Optimization,” AIAA J., **39**(5), pp. 877–884.
[57] Becker, G., Schäfer, M., and Jameson, A., 2011, “An Advanced NURBS Fitting Procedure for Post-Processing of Grid-Based Shape Optimizations,” AIAA Paper No. 2011-891.
[58] Agromayor, R., Anand, N., Müller, J.-D., Pini, M., and Nord, L. O., 2021, “A Unified Geometry Parametrization Method for Turbomachinery Blades,” Comput.-Aided Des., **133**, p. 102987.
[59] Banović, M., Mykhaskiv, O., Auriemma, S., Walther, A., Legrand, H., and Müller, J.-D., 2018, “Algorithmic Differentiation of the Open CASCADE Technology CAD Kernel and Its Coupling With an Adjoint CFD Solver,” Optim. Methods Software, **33**(4–6), pp. 813–828.
[60] Pardiñas, Á. Á., Pilarczyk, M., Agromayor, R., and Nord, L. O., 2019, “Design of an Experimental ORC Expander Setup Using Natural Working Fluids,” Proceedings of the Fifth International Seminar on ORC Power Systems, Athens, Greece, Sept. 9–11, pp. 1–8.
[61] Various authors, 2020, “Parablade v1.0,”.
[62] Piegl, L., and Tiller, W., 2012, *The NURBS Book*, 2nd ed., Springer Science & Business Media, Berlin, Germany.
[63] Korakianitis, T., and Papagiannidis, P., 1993, “Surface-Curvature-Distribution Effects on Turbine-Cascade Performance,” ASME J. Turbomach., **115**(2), pp. 334–341.
[64] Geuzaine, C., and Remacle, J.-F., 2009, “Gmsh: A 3-D Finite Element Mesh Generator With Built-In Pre- and Post-Processing Facilities,” Int. J. Numer. Methods Eng., **79**(11), pp. 1309–1331.
[65] Various authors, 2020, “Gmsh v4.6”.
[66] Dwight, R. P., 2009, “Robust Mesh Deformation Using the Linear Elasticity Equations,” Proceedings of the Fourth International Conference on Computational Fluid Dynamics (ICCFD 2006), Ghent, Belgium, pp. 401–406.
[67] Alfonsi, G., 2009, “Reynolds-Averaged Navier–Stokes Equations for Turbulence Modeling,” ASME Appl. Mech. Rev., **62**(4), p. 040802.
[68] Peng, D.-Y., and Robinson, D. B., 1976, “A New Two-Constant Equation of State,” Ind. Eng. Chem. Fundam., **15**(1), pp. 59–64.
[69] Vitale, S., Gori, G., Pini, M., Guardone, A., Economon, T. D., Palacios, F., Alonso, J. J., and Colonna, P., 2015, “Extension of the SU2 Open Source CFD Code to the Simulation of Turbulent Flows of Fluids Modelled With Complex Thermophysical Laws,” AIAA Paper No. 2015-2760.
[70] White, F. M., 2006, *Viscous Fluid Flow*, 3rd ed., McGraw-Hill, Singapore.
[71] Menter, F. R., 1994, “Two-Equation Eddy-Viscosity Turbulence Models for Engineering Applications,” AIAA J., **32**(8), pp. 1598–1605.
[72] Barth, T., 1991, “Numerical Aspects of Computing High Reynolds Number Flows on Unstructured Meshes,” AIAA Paper No. 91-721.
[73] Palacios, F., Alonso, J., Duraisamy, K., Colonno, M., Hicken, J., Aranake, A., Campos, A., 2013, “Stanford University Unstructured (SU^2): An Open-Source Integrated Computational Environment for Multi-Physics Simulation and Design,” AIAA Paper No. 2013-0287.
[74] Economon, T. D., Palacios, F., Copeland, S. R., Lukaczyk, T. W., and Alonso, J. J., 2016, “SU2: An Open-Source Suite for Multiphysics Simulation and Design,” AIAA J., **54**(3), pp. 828–846.
[75] Roe, P. L., 1981, “Approximate Riemann Solvers, Parameter Vectors, and Difference Schemes,” J. Comput. Phys., **43**(2), pp. 357–372.
[76] Vinokur, M., and Montagné, J.-L., 1990, “Generalized Flux-Vector Splitting and Roe Average for an Equilibrium Real Gas,” J. Comput. Phys., **89**(2), pp. 276–300.
[77] Harten, A., and Hyman, J. M., 1983, “Self-Adjusting Grid Methods for One-Dimensional Hyperbolic Conservation Laws,” J. Comput. Phys., **50**(2), pp. 235–269.
[78] van Leer, B., 1979, “Towards the Ultimate Conservative Difference Scheme. V. A Second-Order Sequel to Godunov’s Method,” J. Comput. Phys., **32**(1), pp. 101–136.
[79] van Albada, G. D., van Leer, B., and Roberts, W. W., 1997, “A Comparative Study of Computational Methods in Cosmic Gas Dynamics,” Upwind High-Resolution Schemes, Springer/Berlin, Germany, pp. 95–103.
[80] Kemm, F., 2011, “A Comparative Study of TVD-Limiters—Well-Known Limiters and an Introduction of New Ones,” Int. J. Numer. Methods Fluids, **67**(4), pp. 404–440.
[81] Weiss, J., Maruszewski, J., and Smith, W., 1997, “Implicit Solution of the Navier-Stokes Equations on Unstructured Meshes,” AIAA Paper No. 97-2103.
[82] Mavriplis, D., 2003, “Revisiting the Least-Squares Procedure for Gradient Reconstruction on Unstructured Meshes,” AIAA Paper No. 2003-3986.
[83] Saad, Y., 2003, *Iterative Methods for Sparse Linear Systems*, 2nd ed., Society for Industrial and Applied Mathematics, Philadelphia, PA.
[84] Giles, M. B., 1990, “Nonreflecting Boundary Conditions for Euler Equation Calculations,” AIAA J., **28**(12), pp. 2050–2058.
[85] Giles, M. B., 1991, “UNSFLO: A Numerical Method for the Calculation of Unsteady Flow in Turbomachinery,” Gas Turbine Laboratory, Massachusetts Institute of Technology, Cambridge, MA, Technical Report No. GTL 205.
[86] Saxer, A. P., and Giles, M. B., 1993, “Quasi-Three-Dimensional Nonreflecting Boundary Conditions for Euler Equations Calculations,” J. Propul. Power, **9**(2), pp. 263–271.
[87] Saxer, A. P., and Giles, M. B., 1994, “Predictions of Three-Dimensional Steady and Unsteady Inviscid Transonic Stator/Rotor Interaction With Inlet Radial Temperature Nonuniformity,” ASME J. Turbomach., **116**(3), pp. 347–357.
[88] Albring, T. A., Sagebaum, M., and Gauger, N. R., 2016, “Efficient Aerodynamic Design Using the Discrete Adjoint Method in SU2,” AIAA Paper No. 2016-3518.
[89] Sagebaum, M., Albring, T., and Gauger, N. R., 2018, “Expression Templates for Primal Value Taping in the Reverse Mode of Algorithmic Differentiation,” Optim. Methods Software, **33**(4–6), pp. 1207–1231.
[90] Sagebaum, M., Albring, T., and Gauger, N. R., 2019, “High-Performance Derivative Computations Using CoDiPack,” ACM Trans. Math. Software, **45**(4), pp. 1–26.
[91] Lyness, J. N., and Moler, C. B., 1967, “Numerical Differentiation of Analytic Functions,” SIAM J. Numer. Anal., **4**(2), pp. 202–210.
[92] Squire, W., and Trapp, G., 1998, “Using Complex Variables to Estimate Derivatives of Real Functions,” SIAM Rev., **40**(1), pp. 110–112.
[93] Martins, J. R. R. A., Sturdza, P., and Alonso, J. J., 2003, “The Complex-Step Derivative Approximation,” ACM Trans. Math. Software (TOMS), **29**(3), pp. 245–262.
[94] Kraft, D., 1988, “A Software Package for Sequential Quadratic Programming,” German Test and Research Institute for Aviation and Space Flight, Oberpfaffenhofen, Germany, Technical Report No. DFVLR-FB 88–28.
[95] Various authors, 2020, “Scipy v1.5”.
[96] Kiock, R., Lehthaus, F., Baines, N. C., and Sieverding, C. H., 1986, “The Transonic Flow Through a Plane Turbine Cascade as Measured in Four European Wind Tunnels,” ASME J. Eng. Gas Turbines Power, **108**(2), pp. 277–284.
[97] Hodson, H. P., and Dominy, R. G., 1987, “Three-Dimensional Flow in a Low-Pressure Turbine Cascade at Its Design Condition,” ASME J. Turbomach., **109**(2), pp. 177–185.
[98] Arts, T., and Lambert de Rouvroit, M., 1992, “Aero-Thermal Performance of a Two-Dimensional Highly Loaded Transonic Turbine Nozzle Guide Vane: A Test Case for Inviscid and Viscous Flow Computations,” ASME J. Turbomach., **114**(1), pp. 147–154.

[99] Agromayor, R., and Nord, L. O., 2019, “Preliminary Design and Optimization of Axial Turbines Accounting for Diffuser Performance,” Int. J. Turbomach., Propul. Power, **4**(3), p. 32.

[100] Kacker, S. C., and Okapuu, U., 1982, “A Mean Line Prediction Method for Axial Flow Turbine Efficiency,” ASME J. Eng. Power, **104**(1), pp. 111–119.

[101] Saravanamuttoo, H. I. H., Rogers, G. F. C., and Cohen, H., 2009, *Gas Turbine Theory*, 6th ed., Pearson Education, Harlow, UK.

[102] Bell, I. H., Wronski, J., Quoilin, S., and Lemort, V., 2014, “Pure and Pseudo-Pure Fluid Thermophysical Property Evaluation and the Open-Source Thermophysical Property Library CoolProp,” Ind. Eng. Chem. Res., **53**(6), pp. 2498–2508.

[103] Bücker, D., and Wagner, W., 2006, “Reference Equations of State for the Thermodynamic Properties of Fluid Phase n-Butane and Isobutane,” J. Phys. Chem. Ref. Data, **35**(2), pp. 929–1019.

[104] Vogel, E., Küchenmeister, C., and Bich, E., 2000, “Viscosity Correlation for Isobutane Over Wide Ranges of the Fluid Region,” Int. J. Thermophys., **21**(2), pp. 343–356.

[105] Perkins, R. A., 2002, “Measurement and Correlation of the Thermal Conductivity of Isobutane From 114 K to 600 K at Pressures to 70 MPa,” J. Chem. Eng. Data, **47**(5), pp. 1272–1279.

[106] Denton, J. D., 1993, “The 1993 IGTI Scholar Lecture: Loss Mechanisms in Turbomachines,” ASME J. Turbomach., **115**(4), pp. 621–656.